The Astrophysical Journal, 991:104 (13pp), 2025 September 20 https://doi.org/10.3847/1538-4357/adf8d9

Exploring SEP Transport in Widespread Events with Different Heliospheric Current Sheet Models

C. O. G. Waterfall[1,2], G. A. de Nolfo[1], A. Hutchinson[1], D. da Silva[1,3], S. Wallace[4], S. Dalla[5], and J. G. Mitchell[1]
[1] Heliophysics Division, NASA Goddard Space Flight Center, Greenbelt, MD, USA
[2] University Corporation for Atmospheric Research, Boulder, CO 80301, USA
[3] University of Maryland, Baltimore County, USA
[4] Department of Physical Sciences, Embry-Riddle Aeronautical University, 1 Aerospace Blvd., Daytona Beach, FL 32114, USA
[5] Jeremiah Horrocks Institute, University of Central Lancashire, Preston PR1 2HE, UK
Received 2025 May 23; revised 2025 July 21; accepted 2025 July 23; published 2025 September 18

Abstract

Understanding solar energetic particle transport in wide-longitude events remains a significant question in heliophysics. By utilizing the increasing number of available observers at various heliographic distances and longitudes, such as Parker Solar Probe and Solar Orbiter, we are able to further our understanding of these widespread events. This study presents 3D test particle modeling of three widespread events during the Parker era, each detected by at least four observers. The role of the heliospheric current sheet (HCS) in transporting particles to the wide longitudes observed in these events is evaluated. A newly updated and more sophisticated HCS model is used, incorporating three different configurations derived from the Wilcox Solar Observatory, Air Force Data Assimilative Photospheric Flux Transport, and Solar Dynamics Observatory/Helioseismic and Magnetic Imager (HMI) data (via Predictive Science, PSI) for each event. The modeled proton flux profiles at each observer location are compared against energetic proton measurements for each HCS configuration. We find that inclusion of the HCS is essential to reproduce both the wide longitudinal spread of particles and the observed flux profiles in all three events. For events with longitudinal separations exceeding 100°, the most intense fluxes, both observed and modeled, are associated with observers located nearest to the HCS. This is observed for the 2023 March 13 event, where two observers were located closer in longitude and radial distance than other observers to the source region, yet observed no solar energetic particle signatures due to their lack of proximity to the HCS. Among the three configurations, the HMI-PSI-derived HCS consistently yields the best agreement between observed and modeled flux profiles.

Unified Astronomy Thesaurus concepts: Solar energetic particles (1491); Solar activity (1475); Solar particle emission (1517); Space weather (2037); Heliosphere (711)

1. Introduction

Solar energetic particles (SEPs) are often detected throughout the heliosphere following large solar eruptive events; however, the mechanisms for this particle transport and how these particles are distributed throughout interplanetary space remain open questions. With the rise in SEP observations at multiple locations by recent spacecraft such as Parker Solar Probe (A. Kouloumvakos et al. 2020; J. Mitchell et al. 2021) and Solar Orbiter (R. Bučík et al. 2023), as well as the existing fleet of 1 au observers (GOES, STEREO, etc.), we are now uniquely positioned to investigate the nature of wide-longitude SEP events and the influence of heliospheric structures, such as the heliospheric current sheet (HCS), on particle propagation.

There have been several wide-longitude events already reported in tthe literature. A wide-longitude SEP event refers to the detection of SEPs over longitudinal separations typically exceeding 90°–120°. The first widespread event of solar cycle 25 occurred on 2020 November 29 and was detected by Parker Solar Probe, Solar Orbiter, and STEREO-A as well as numerous near-Earth spacecraft. This event was associated with a large coronal mass ejection (CME) and M4-class solar flare, resulting in a longitudinal spread of SEPs over 230° at 1 au (A. Kollhoff et al. 2021). Another frequently discussed widespread event is that of 2021 April 17 (N. Dresing et al. 2023). This event was detected over a range of radial distances between 0.42 and 1 au and longitudinally over 110° by spacecraft including BepiColombo as well as those listed above. The spread of particles during the event of 2021 April 17 has been attributed to multiple SEP injections from the same location over a short period of time. However, many widespread events are often characterized by a large solar eruption including a wide and fast CME and (when observed in front of the limb) an intense M- or X-class solar flare. The widespread events mentioned here, as well as others detected so far during solar cycle 25, are listed in a new catalog as part of the SERPENTINE project (N. Dresing et al. 2024).

A notable widespread event occurred 2021 October 28, triggering GLE 73. This event represents the most spatially comprehensive SEP detection during solar cycle 25 so far, observed simultaneously by six key spacecraft spanning a wide range of radial and longitudinal positions. It was detected by all six key observers relevant to this research: Earth, Parker, Solar Orbiter, STEREO, Bepi, and Mars. (This is not the only widespread SEP event detected at Mars during solar cycle 25, with others discussed by J. Semkova et al. 2023).

The HCS, a surface of magnetic polarity reversal in the heliosphere, can act as a channel for charged particles to drift across. The HCS is a possible contributor to the propagation of particles across the average interplanetary magnetic field (IMF) and thus the detection of widespread events. When charged particles come within about one Larmor radius of the

HCS, their motion is drastically modified: the guiding center approximation breaks down and their trajectory is no longer of helical shape (E. H. Levy 1976; R. Burger et al. 1985). The particles start drifting along the HCS and move across the magnetic field efficiently. This effect was recognized as important in the propagation of galactic cosmic rays (e.g., J. Kota & J. R. Jokipii 1983) and more recently SEPs (M. Battarbee et al. 2018a; S. Dalla et al. 2020). It is routinely included in cosmic-ray modulation models.

The HCS drift only becomes active when particles reach the HCS: When the SEP particle source is located far from it, drifts associated with the gradient and curvature of the IMF or other perpendicular transport mechanisms (e.g., S. Dalla et al. 2013; J. van den Berg et al. 2020; T. Laitinen & S. Dalla 2025 and references therein) may help particle propagation to the HCS, at which point HCS drift takes place. If the source is too far, particles may never reach the HCS. When HCS and gradient/curvature drift effects are taken into account, a dependence of SEP spatial distributions in the heliosphere on the polarity of the IMF (A^+ or A^-) becomes apparent (e.g., S. Dalla et al. 2020).

The role of the HCS has previously been explored in ground level enhancement (GLE) events by C. O. Waterfall et al. (2022). It was seen that for the largest GLE events, an injection region close to the HCS largely aided in transporting particles toward the observer and over extensive longitudinal ranges. Various parameters were varied in the simulations, including the injection width and the scattering mean free path; however, the addition of the HCS was the dominant factor in particle transport and rapid onset times. GLE 73 was extensively researched by A. Kouloumvakos et al. (2024), including test particle modeling of the event both with and without the HCS. It was seen that when the HCS was removed from the model, the particles failed to be transported to the more widely separated locations, that is, Mars and Bepi.

Other possible mechanisms to explain widespread particle events include wide CME shocks and perpendicular diffusion, as well as particle transport along the HCS (R. Gómez-Herrero et al. 2015). Although many studies have employed particle transport simulations to investigate specific SEP events (e.g., M. Battarbee et al. 2018b; C. O. Waterfall et al. 2022), the HCS is often omitted from models, despite its demonstrated importance in extreme events. The HCS is a dynamic and complex environment, increasingly so around solar maximum, and its possible role in transporting particles cannot be ignored. There are several models that utilize various observations of the solar magnetic field to produce magnetograms and maps of the HCS. For example, Wilcox Solar Observatory (WSO) calculates their coronal magnetic field from photospheric field observations with a potential field model. Previously, simulations of GLE events by C. O. Waterfall et al. (2022) used the HCS configuration provided by WSO. However, other models, such as Air Force Data Assimilative Photospheric Flux Transport (ADAPT) and the configuration derived from Solar Dynamics Observatory (SDO)/Helioseismic and Magnetic Imager (HMI) observations used in A. Kouloumvakos et al. (2024), are available. Previous work has not accounted for the varying current sheet configurations and how different models may affect particle transport simulations. An updated version of the HCS model used in C. O. Waterfall et al. (2022) is employed in this work to simulate three wide-longitude SEP events and compare model flux profiles with observations. The model has been modified to incorporate a more sophisticated description of the HCS, rather than the approximate fit used previously. A primary goal of this work is to assess whether test particle modeling can help constrain which HCS model configuration best reproduces the observed SEP flux profiles. Section 2 details the different HCS models to be used. Section 3 outlines the events to be simulated and how they were selected. The results from the test particle modeling of these events is given in Section 4, and the overall results and conclusions are discussed in Section 5.

2. Different HCS Configurations

Accurately modeling the HCS is crucial for understanding how energetic particles are transported across wide longitudinal ranges. The HCS is the surface that separates regions of opposite magnetic polarity in the solar wind, and its warped, dynamic structure can act as a conduit for particle propagation over large angular separations. In this study, we evaluate three distinct HCS configurations derived from different models and magnetogram sources: the WSO model (http://wso.stanford.edu), the ADAPT model (http://connect-tool.irap.omp.eu), and the model derived from SDO/HMI data produced by Predictive Science Inc. (PSI) (https://www.predsci.com/hmi/).

2.1. HCS Models and Magnetic Field Sources

The WSO HCS configuration is calculated using a potential field source surface (PFSS) model based on daily line-of-sight photospheric magnetic field observations. The coronal magnetic field is extrapolated under the assumption that it becomes purely radial at a source surface height of 2.5 $R_\odot$ (J. T. Hoeksema et al. 1983). This model has been widely used in past studies of SEP events, including GLE simulations by C. O. Waterfall et al. (2022), and serves as a baseline reference.

The ADAPT model incorporates flux transport and data assimilation techniques to produce a time-dependent map of the photospheric magnetic field (C. N. Arge et al. 2013). By assimilating multiple magnetograms over time and evolving the field using surface flows, the ADAPT model attempts to better capture the dynamic state of the solar surface. The HCS derived from ADAPT outputs is expected to reflect more realistic temporal variability than static models.

The SDO/HMI-based HCS configuration used in this study is derived from MHD extrapolations provided by PSI (hereafter referred to as the HMI/PSI model). These models use synoptic vector magnetograms from the HMI on board SDO to compute the large-scale coronal magnetic field. This approach offers improved spatial fidelity and more detailed magnetic field structure compared to synoptic maps like those from WSO. Like the other models, the HMI/PSI configuration assumes a source surface height of 2.5 $R_\odot$ to match previous simulation setups.

2.2. Importance of HCS Configuration

One of the central goals of this study is to investigate how differences in HCS configuration affect SEP transport in widespread events. The shape, orientation, and spatial extent of the HCS can vary significantly depending on the model used. These differences can result in changes to both the injection region's proximity to the HCS and the location of the observers with respect to it, potentially altering the longitudinal spread and intensity of detected particle fluxes.

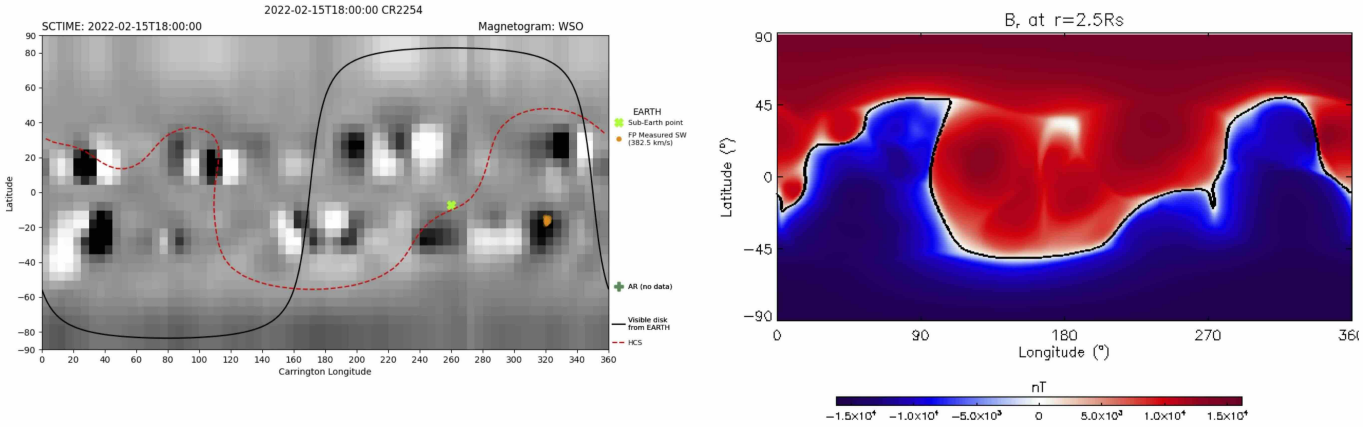

Figure 1. Different HCS configurations for 2022 February 15. Example Carrington maps showing the configuration of the HCS generated with ADAPT (left, red dashed line, from http://connect-tool.irap.omp.eu) and HMI/PSI measurements at 2.5 $R_{\odot}$ (right, black line, from https://www.predsci.com/hmi/).

Figure 1 illustrates the HCS configurations for a sample event as derived from the ADAPT and HMI/PSI models. Each model yields a different current sheet morphology, which in turn leads to varying magnetic connectivity between the source region and the observer locations. By simulating each event with all three HCS configurations, we evaluate how sensitive the resulting particle transport is to these model-dependent differences.

In particular, we assess whether the injection region's distance from the HCS in each configuration correlates with the ability to reproduce the observed SEP fluxes. Events where the injection occurs near the HCS may see enhanced particle access to otherwise poorly connected observers, whereas configurations placing the HCS farther from either the source or the observer may inhibit transport.

3. Widespread Events

The wide-longitude SEP events selected for this study were chosen based on several criteria. First, an increase in energetic protons had to be detected at four or more observers from the following list: STEREO-A, Earth (e.g., GOES, Solar and Heliospheric Observatory, SOHO), Parker Solar Probe, Solar Orbiter, Mars, and BepiColombo. Second, at least two of these observers had to be separated in longitude by a minimum of 90°. Finally, to leverage recent high-quality data from Parker Solar Probe, Solar Orbiter, and the HCS models discussed in Section 2, only events occurring from 2019 onward were considered.

Information on candidate events was compiled from several existing event catalogs (J. Mitchell et al. 2023; N. Dresing et al. 2024). Preference was given to events that showed clear increases in higher-energy proton channels (e.g., the 60–100 MeV range on STEREO), as well as events that had not been previously modeled in detail (excluding, for instance, the well-studied 2021 October 28 GLE event; A. Kouloumvakos et al. 2024). Based on these criteria, three events were selected, listed in Table 1. Each of these events was associated with a fast and wide CME. (Note that the large widespread SEP events of 2024, including GLE 74, had not occurred when this research was conducted but will be evaluated in a future study.)

Figure 2 presents the HCS configuration at 2.5 $R_{\odot}$ for each of the three selected events, using the WSO, ADAPT, and HMI/PSI models. While there is general agreement in the large-scale structure between the three models, noticeable differences are present in certain longitudinal regions. For example, in the 2022 February 15 event (top panel), the WSO and ADAPT models diverge significantly in the 100°–200° longitude range. Overall, the HCS appears smoother and more idealized in the WSO and ADAPT models, whereas the HMI/PSI configuration exhibits finer structure and increased complexity, particularly for the 2022 March 14 event (middle panel). This reflects the more detailed input data and higher resolution of the HMI-derived model.

The most disturbed current sheet morphology is seen in the 2023 March 13 event (bottom panel), with highly tilted and irregular HCS structures across all models. These events occurred during the rising phase of solar cycle 25, during which the HCS becomes increasingly warped.

Also shown in Figure 2 are the source surface foot points of the observers, computed using three separate methods. The first uses ADAPT-based connectivity (triangles) from http://connect-tool.irap.omp.eu. The second uses a standard Parker spiral calculation using the measured or assumed solar wind speed (circles) (J. Gieseler et al. 2023). The third approach we use to derive the instantaneous spacecraft connectivity for each SEP event uses the Wang–Sheeley–Arge (WSA) (C. Arge & V. Pizzo 2000; C. N. Arge et al. 2003; C. Arge et al. 2004; S. McGregor et al. 2008) model. WSA is an empirical and physics-based model that derives the global coronal field using a coupled set of potential-field-type models. The first is a traditional magnetostatic PFSS model (K. H. Schatten et al. 1969; M. D. Altschuler & G. Newkirk 1969; Y.-M. Wang & N. Sheeley 1992), which determines the coronal field out to the source surface height. The PFSS solution then is used as input into the Schatten current sheet model (K. H. Schatten 1971), to derive a more realistic magnetic field topology of the upper corona. In this work, we derive the Schatten current sheet solution out to 5 $R_{\odot}$, which is appropriate for applications of deriving spacecraft connectivity since WSA is magnetostatic and is designed to be most accurate in low beta regimes (C. Arge et al. 2004). The instantaneous connectivity between a satellite of interest and the solar surface is determined by back-projecting the satellite's location as if it were positioned on the grid cells (i.e., one for each field line endpoint) at the model outer coronal boundary, which has a uniform resolution of 2° for this study. This is accomplished using the observed solar wind velocity and an assumption of Parker spiral

Table 1
Table of Wide-longitude SEP Events Detected in the Parker Era by Multiple Spacecraft

Date	Flare Class	Flare Carr Longitude	CME speed (km s^{-1})	Earth	STA	Parker	SolO	Bepi
15 Feb 22	BL	97	2376	x	x	x	small	x
14 Mar 22	M1.4	14	740	x	x	x	x	⋯
13 Mar 23	BL	25	1669	x	x	x		⋯

Note. Confirmed events are marked as "x," with small events marked as such. The three events are all associated with behind-limb or near-limb events; however, are all detected at Earth. Information on observations and the solar eruption is obtained from J. Semkova et al. (2023) and L. Khoo et al. (2024) as well as the SERPENTINE widespread catalog (N. Dresing et al. 2024).

structure for the IMF. A value of 500 km s^{-1} is used when a solar wind velocity measurement is not available. Once this is accomplished, the magnetic field can be traced from the grid cell centers associated with the spacecraft's location at 5 $R_\odot$ to the solar surface at 1 $R_\odot$. This approach is repeated for WSA solutions within a window of time around the target time (±12 hr) to collect a larger set of solutions. This time window approach was previously developed for solar wind connectivity (D. Da Silva et al. 2023) and is justified because the WSA model is often accurate but delayed within this timescale.

In this work, the WSA model is driven by global and synchronic photospheric field maps generated by the ADAPT (C. N. Arge et al. 2013) model, using magnetograms from the Global Oscillation Network Group (J. Harvey et al. 1996). ADAPT uses magnetic flux transport based on the Worden and Harvey (J. Worden & J. Harvey 2000) model to account for solar time-dependent evolution (i.e., differential rotation, meridional and supergranulation flows), even when observations are not available. Flux transport models are currently the only way to represent the photospheric magnetic field instantaneously since we do not routinely observe the Sun's far side and poles. This approach is unique relative to the one used in the other models in this study, which use traditional photospheric field data products that are diachronic in nature (i.e., typically represent a time history of central meridian evolution over a Carrington rotation).

Furthermore, ADAPT produces an ensemble of 12 maps (or realizations) for any given moment in time that best represents the uncertainty in the global photospheric magnetic field distribution. The ADAPT inputs to WSA are varied into 12 ensemble realizations, which result in the same amount of WSA magnetic field solutions and final source locations per time step.

For the 2022 February 15 event, two distinct groups of observers emerge. Bepi and Mars are located close in longitude to the source region, while Earth, Solar Orbiter, and STEREO-A are widely separated by up to 200°. Large discrepancies are seen between foot point methods, particularly between the Parker spiral and ADAPT/WSA-ENLIL models. In many cases, the ADAPT and WSA-derived foot points lie closer to the HCS or to the injection region, emphasizing the importance of considering multiple mapping techniques.

Similar patterns are observed for the 2022 March 14 event. Parker and Mars lie near both the HCS and the inferred source region, while Bepi, Solar Orbiter, and STEREO-A are more longitudinally displaced. The 2023 March 13 event features the most complex HCS structure. Interestingly, BepiColombo and Solar Orbiter appear closer in longitude and latitude to the source region than Earth and STEREO yet remain far from the HCS in all foot point configurations. In contrast, Earth and STEREO-A, although more separated longitudinally from the source, are positioned nearer to the HCS.

As particle drift along the HCS is expected to facilitate transport across wide longitudes, these positional differences suggest that observers closer to the HCS may detect enhanced fluxes, even if they are longitudinally distant from the source region. It is important to note, however, that the observer foot points are not directly used as inputs to the test particle model. Only the injection location is fixed. Observer fluxes are instead calculated at their actual heliocentric distances, allowing the particle transport simulation to reflect their real spatial context. Still, the foot point mappings are included here to explore potential correlations between modeled magnetic connectivity and the observed proton flux profiles.

4. Modeling

4.1. Test Particle Model

The three events listed in Table 1 were simulated using a 3D full orbit test particle code originally developed by S. Dalla & P. Browning (2005). The code solves the relativistic equation of motion for charged test particles in prescribed electric and magnetic fields, given by

$$\frac{d\boldsymbol{p}}{dt} = q\left(\boldsymbol{E} + \frac{\boldsymbol{p}}{\mathrm{cm}_0\gamma} \times \boldsymbol{B}\right), \tag{1}$$

where $\boldsymbol{p}$ is the particle's momentum, t is time, q its charge, m_0 its rest mass, γ its Lorentz factor, and c the speed of light. To describe the heliospheric environment, the code uses expressions for the large-scale fields given by the Parker spiral magnetic field and the solar wind electric field, $\boldsymbol{E} = -\boldsymbol{v}_{\mathrm{sw}}/c \times \boldsymbol{B}$, with $\boldsymbol{v}_{\mathrm{sw}}$ the solar wind velocity, as follows:

$$\boldsymbol{B} = B_0 \frac{r_0^2}{r^2}\boldsymbol{e}_r - \frac{B_0\, r_0^2\, \Omega}{v_{\mathrm{sw}}} \frac{\sin\theta}{r}\boldsymbol{e}_\phi \tag{2}$$

and

$$\boldsymbol{E} = -\frac{\Omega\, B_0 r_0^2}{c} \frac{\sin\theta}{r}\boldsymbol{e}_\theta, \tag{3}$$

where (r, θ, ϕ) are heliocentric spherical coordinates with r the radial distance, θ the colatitude, and ϕ the longitude, with $\boldsymbol{e}_r$, $\boldsymbol{e}_\theta$, and $\boldsymbol{e}_\phi$ as the corresponding unit vectors (M. S. Marsh et al. 2013). The constant B_0 gives the magnitude of $\boldsymbol{B}$ at a reference distance r_0, and Ω is the solar rotation rate. The solar wind flow is assumed to be radial, uniform, and time independent. The sign of the magnetic field is determined by the constant B_0, which changes sign at the HCS. The HCS is implemented as a

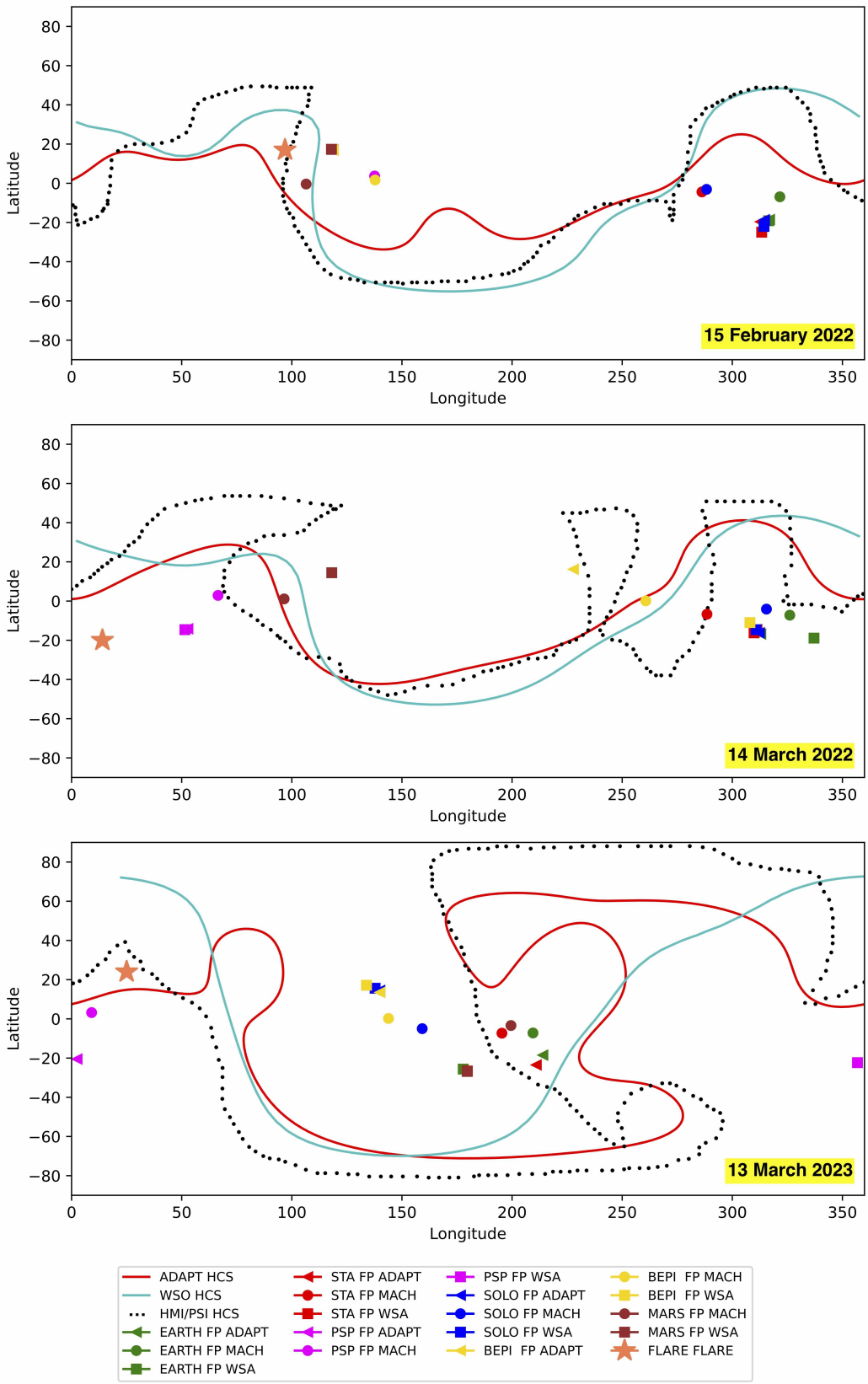

Figure 2. Combined HCS configurations from ADAPT (red), HMI/PSI (black dotted), and WSO (blue) for the three widespread SEP events: 2022 February 15 (top), 2022 March 14 (middle), and 2023 March 13 (bottom). All three show the associated flare as the orange star. The source surface foot points of the observers are shown as symbols. Different models show different foot points, e.g., square: WSA; triangle: ADAPT; circle: standard Parker spiral from Solar-MACH. (If an observer is not shown, no data were available for that model.)

3D surface derived from synoptic or MHD models (WSO, ADAPT, HMI/PSI), and its geometry is directly integrated into the simulation, enabling precise evaluation of particle interactions with the HCS structure. At the HCS, where the magnetic polarity reverses, drifts become especially pronounced, enabling protons to traverse longitudinal distances far beyond what is expected from scatter-dominated diffusion alone.

Being a full orbit test particle simulation, the model naturally includes guiding center drifts associated with the curvature and gradient of $\boldsymbol{B}$, as well as HCS drift due to the reversal of the magnetic field direction at the HCS. The effects of turbulence on the particle propagation are described by means of a so-called ad hoc scattering approach, in which random isotropic scattering of the particle's velocity is implemented, with scattering times drawn from a Poisson distribution and compatible with a scattering mean free path set as input to the code (M. S. Marsh et al. 2013). The mean free path, λ, is set to 0.3 au, consistent with values derived from large SEP and GLE event analyses (J. W. Bieber et al. 2002, 2004; A. Sáiz et al. 2005). In the model, the equations of motion are solved for a population of particles with prescribed initial locations within an injection region and specified energy spectrum. The model has been extensively applied to various heliospheric environments and SEP events (M. Battarbee et al. 2018a, 2018b; S. Dalla et al. 2020; C. O. Waterfall et al. 2022).

Other mechanisms of cross-field transport, such as magnetic field line meandering or small-scale turbulence, are not currently included in this model. While these effects are important and have been studied extensively (e.g., T. Laitinen et al. 2016, 2023), their omission is not expected to significantly impact the interpretation of these specific events and is discussed further in Section 5.

A key improvement in this work, compared to previous simulations that included the HCS, is the ability to directly integrate the 3D coordinates of each HCS model into the particle transport simulation. This enables the particle code to use the precise position of the HCS at any given point, rather than relying on idealized or smoothed approximations. As a result, particles can be injected closer to or farther from the HCS based on the actual magnetic configuration for each event, and their subsequent transport reflects this localized structure.

All events were modeled using the same set of initial injection parameters: instantaneous injection of protons at 2 $R_\odot$ from the center of the Sun, a power-law energy spectrum with an index of 1.5, proton energies between 10 and 1000 MeV, and an injection width of 30° × 30°. The duration of the simulation is 72 hr. The injection location is based on the flare or active region associated with each event, marked by a star in Figure 2. Solar wind speed values are taken from in situ observations where available; otherwise, a nominal value of 400 km s^{-1} is used.

4.2. 2022 February 15

The wide-longitude SEP event of 2022 February 15 was associated with a major solar eruption that occurred just behind the solar limb around 21:50 UTC. Although the flare magnitude could not be directly measured by Solar Orbiter due to its vantage point, the associated CME was fast and wide, with an estimated peak speed of 2376 ± 166 km s^{-1} (L. Khoo et al. 2024). The flare longitude is estimated from the previously observed active region (B. Sánchez-Cano et al. 2023). The event

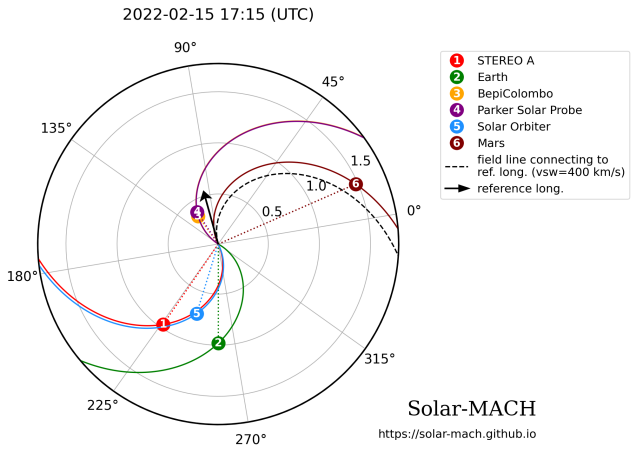

Figure 3. The longitudinal configuration of spacecraft (colored circles) and associated flare (black arrow) for the widespread SEP event of 2022 February 15, generated using the Solar-MACH online tool (J. Gieseler et al. 2023).

was detected sequentially across the heliosphere, with initial observations at Parker Solar Probe and Mars, followed by more gradual onsets at Earth, Solar Orbiter, and STEREO-A the following day (B. Sánchez-Cano et al. 2023; J. Semkova et al. 2023). The spacecraft distribution is shown in Figure 3.

At the time of the event, the HCS was moderately disturbed, with tilt angles exceeding 30° in certain longitudinal regions across all three HCS models. Figure 4 shows the modeled cumulative 72 hr proton (10–1000 MeV) crossing maps at 1 au for each HCS configuration (WSO, ADAPT, and HMI/PSI), as well as a simulation without the HCS. These cumulative maps shown throughout this study represent the total number of simulated protons crossing 1 au at different heliographic longitudes and latitudes. Each pixel value reflects the number of particle crossings detected over the full event duration. These values are displayed on a logarithmic scale to emphasize both strong and weak particle access regions. While not directly equivalent to observed fluxes, instead displaying model particle counts, these maps serve as a spatial diagnostic of SEP transport efficiency. In particular, they reveal how different HCS geometries enable or inhibit proton access to specific longitudes. Regions of higher cumulative counts indicate more favorable drift trajectories or magnetic connectivity from the injection site to 1 au, making these maps a useful proxy for assessing longitudinal spread. Colored squares indicate the heliographic longitude and latitude of each observer. Although the map shows particle crossings at 1 au, observer positions are based on their true position at the time of the event.

These crossing maps reveal that the inclusion of the HCS enables extensive longitudinal transport of particles. All three HCS configurations produce proton crossings spanning nearly 360° at 1 au. In contrast, the no-HCS scenario fails to deliver significant particle counts to widely separated observers such as Earth, STEREO-A, and Solar Orbiter. This highlights the importance of HCS-driven drift in enabling efficient cross-field transport, particularly under the positive IMF polarity (A+), which favors westward drift along the HCS.

Notably, the WSO model shows reduced counts at the more distant observers, whereas both the ADAPT and HMI/PSI configurations facilitate efficient particle transport toward these locations. This suggests that finer-scale HCS features, captured more accurately in the ADAPT and HMI/PSI models, may play a role in connecting distant observers to the source region.

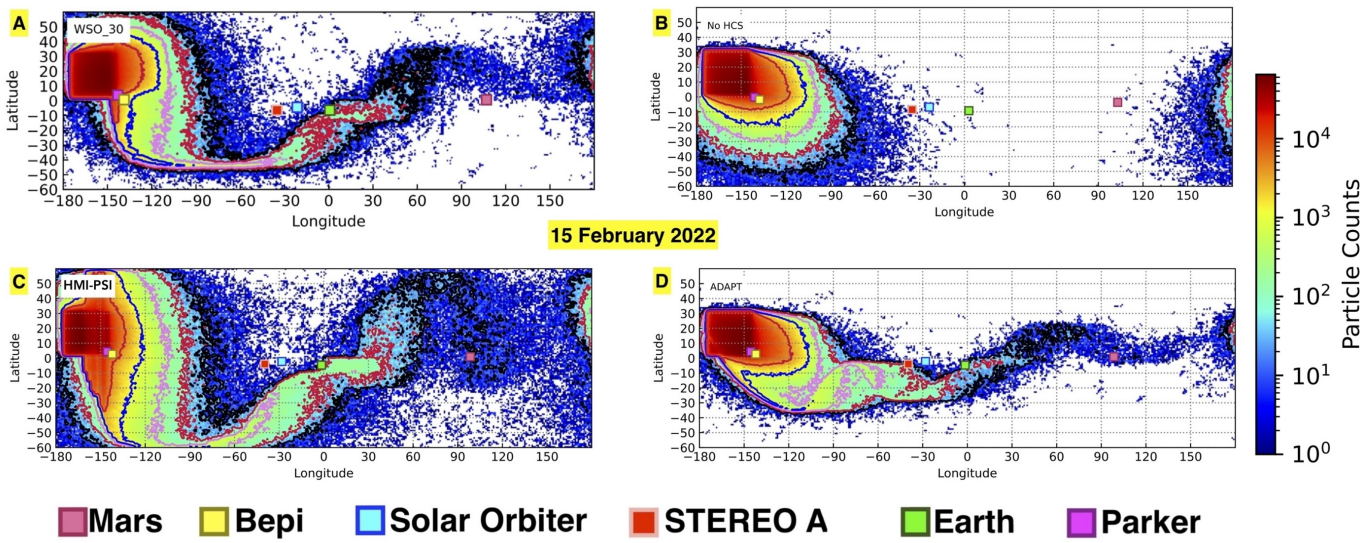

Figure 4. Cumulative 1 au proton crossing maps over 72 hr for (a) ADAPT HCS configuration, (b) no HCS, (c) HMI-PSI HCS, and (d) WSO HCS for 2022 February 15. Colored square markers indicate the actual heliospheric location of each observer for visualization purposes, in Carrington longitude and latitude. These are not Parker spiral foot points projected to 1 au but rather the spacecraft's true positions, which may be closer to 1 au (as is often true for Parker Solar Probe in this study); Bepi (yellow), Solar Orbiter (blue), STEREO-A (red), Earth (green), Parker Solar Probe (pink), Mars (brown). The injection location in each case is taken as the approximate location of the solar flare.

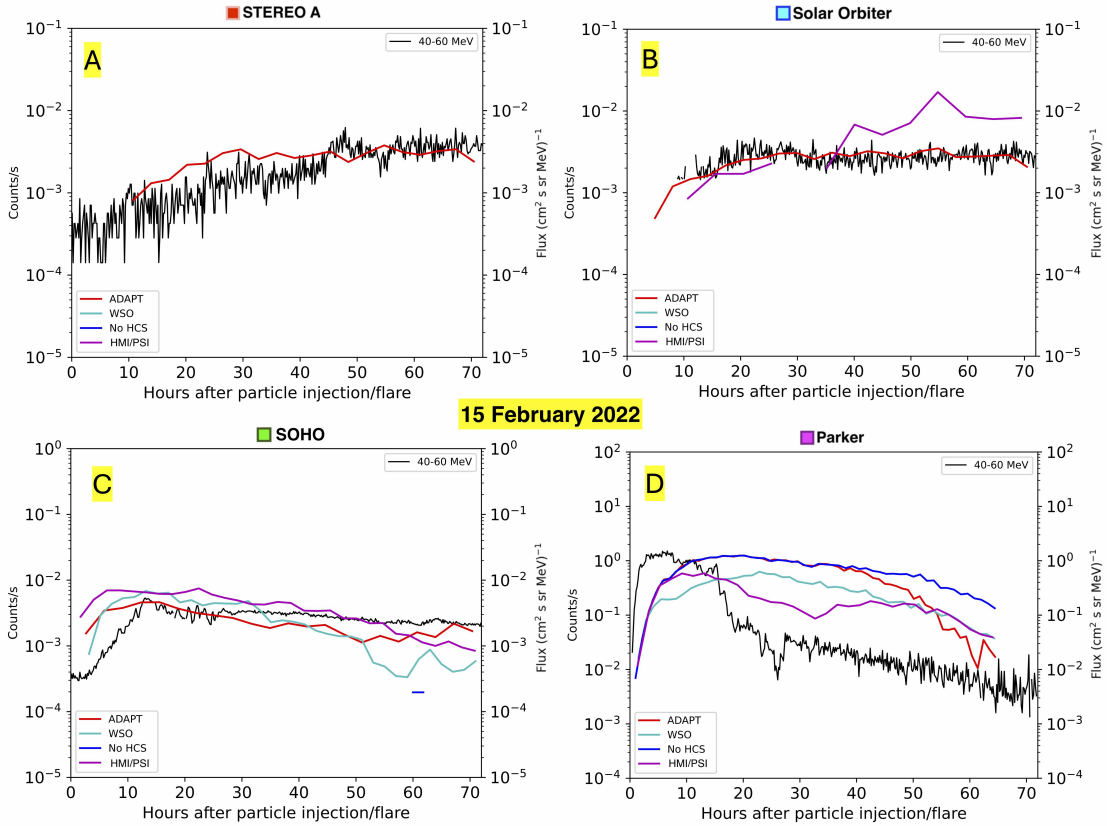

Figure 5. Observed 40–60 MeV proton flux profiles for 2022 February 15 for (A) STEREO-A, (B) Solar Orbiter, (C) SOHO, and (D) Parker Solar Probe (black lines). Model flux profiles obtained from the observers' heliospheric location are overlaid on each plot corresponding to the different HCS configurations: purple, HMI/PSI; red, ADAPT; cyan, WSO; blue, no HCS. Each plot shows flux profiles over 72 hr from the time of injection/flare start time. Model count rates and proton flux rates are shown on the left and right vertical axes, respectively.

4.2.1. Observations and Modeled Flux Profiles

The modeled proton flux time profiles over 72 hr are shown in Figures 5 and 6, with each panel corresponding to a different observer. Flux profiles are plotted for all three HCS configurations, as well as for the simulation without the HCS. These are compared with observed fluxes for energy channels matched to the simulation output. All observational spacecraft data in the 40–60 MeV range used here have been intercalibrated.

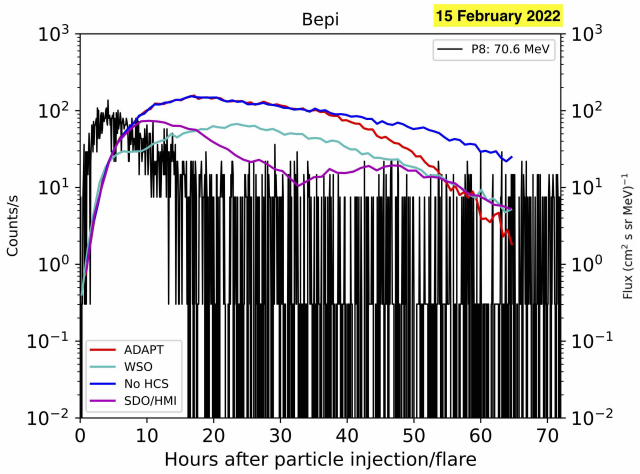

Figure 6. Observed (black) and model flux profiles (zero counts) for BepiColombo for 2022 February 15. Plot information is the same as in Figure 5.

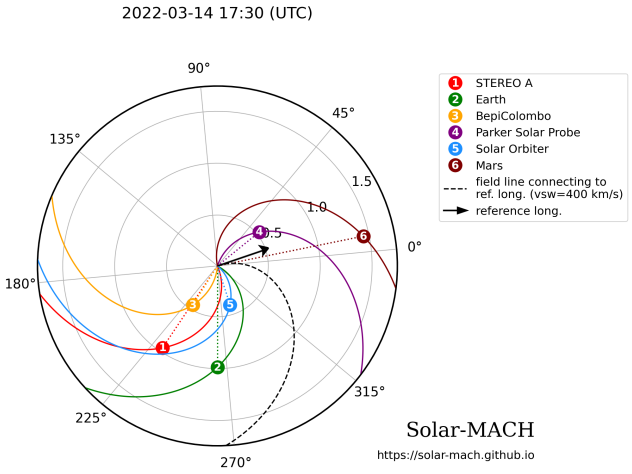

Figure 7. The longitudinal configuration of spacecraft (colored squares) and associated flare (black arrow) for the widespread SEP event of 2022 March 14, generated using the Solar-MACH online tool (J. Gieseler et al. 2023).

That is to say they have been scaled from their raw observation values according to a method detailed in A. Hutchinson et al. (2025, in preparation). The values by which these data have been scaled were determined by considering reservoir events where the profiles should converge to similar values of observed flux. This method provides single intercalibration factors (ICFs) that are the median ICFs derived from a number of reservoir events. As such there are uncertainties associated with these data, which alter the flux magnitude. However, the overall shape of the profiles remains the same. The spacecraft ICFs are with respect to SOHO observations, meaning the SOHO data are the raw observations (ICF for SOHO is 1.0). Where spacecraft do not have channels that cover 40–60 MeV exactly, artificial channels were derived from integrating the energy spectrum; for more information, please see A. Hutchinson et al. (2025, in preparation).

At observers located close to the source region (e.g., Parker and BepiColombo, see Figure 6), all models (including the one without the HCS) produce strong flux enhancements. However, the inclusion of the HCS leads to an earlier onset and sharper rise in the profiles. This is particularly clear at Parker, which shows the earliest observed peak and highest count rates, well captured by the model.

In contrast, for observers farther from the source in longitude (STEREO-A, SOHO, and Solar Orbiter), the inclusion of the HCS is critical to match the observed profiles. The no-HCS simulations fail to produce significant particle counts at these locations. Among the HCS configurations, ADAPT and HMI/PSI provide more accurate timing and profile shapes, suggesting that their more detailed field structures allow for enhanced drift-driven access to these observers.

An interesting case is SOHO, which despite being longitudinally similar to STEREO-A and Solar Orbiter, shows an earlier onset and stronger flux profile. Figure 4 reveals that SOHO lies more directly on the HCS at 1 au in all three models, facilitating more efficient particle access via drift. This supports the idea that magnetic connectivity via the HCS can play a dominant role, even for observers far from the source longitude.

For Parker and BepiColombo, the no-HCS model exhibits prolonged elevated fluxes, likely due to Parker spiral curvature and gradient drifts delivering particles directly. When the HCS is included, these particles are more rapidly redistributed across the heliosphere, resulting in a sharper and earlier peak at these observers.

It is not straightforward to determine whether one HCS configuration outperforms the others in this event. All three improve the match to observations relative to the no-HCS case, but ADAPT and HMI/PSI offer slightly better agreement in flux amplitude and onset time at the more distant observers. This reflects the broader structure and finer detail captured in those configurations.

4.3. 2022 March 14

The wide-longitude SEP event of 2022 March 14 was associated with a solar eruption that began around 17:13 UTC, originating just behind the western limb. Based on STIX observations from Solar Orbiter, the flare magnitude was estimated as M1.4, although this may be an underestimate due to the limb location. A flare Carrington longitude of 14° is assumed from J. Gieseler et al. (2023). The event was accompanied by a partial halo CME with a speed of approximately 740 km s^{-1}. The spacecraft distribution is shown in Figure 7.

Protons were first detected by Parker Solar Probe at 17:42 UTC (N. Dresing et al. 2024), followed shortly by an increase at Mars at 17:55 UTC (J. Semkova et al. 2023). Later onsets were recorded at Solar Orbiter, STEREO-A, and Earth.

The HCS configurations for this event are shown in the middle panel of Figure 2. There is broad agreement between the WSO and ADAPT models, while the HMI/PSI configuration displays more intricate structure and greater latitudinal variability.

Figure 8 presents the cumulative 72 hr 1 au proton crossing maps for the three HCS configurations, along with a simulation with no HCS. The IMF polarity was A+, and all simulations that include the HCS show extensive longitudinal spreading of particles. The HMI/PSI model, in particular, exhibits substantial latitudinal particle spread, while WSO and ADAPT demonstrate efficient HCS-driven transport across nearly all longitudes.

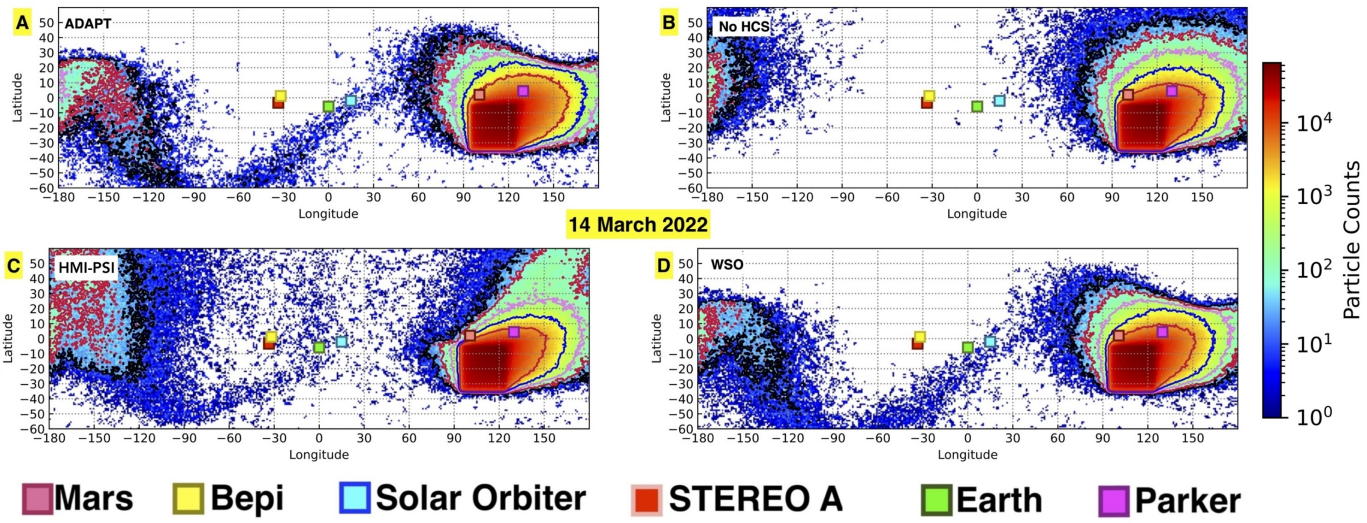

Figure 8. Cumulative 1 au proton crossing maps over 72 hr for (a) ADAPT HCS configuration, (b) no HCS, (c) HMI-PSI HCS, and (D) WSO HCS for 2022 March 14. Heliospheric observer locations are shown as colored squares: Bepi (yellow), Solar Orbiter (blue), STEREO-A (red), Earth (green), Parker Solar Probe (pink), Mars (brown). The injection location in each case is taken as the approximate location of the solar flare.

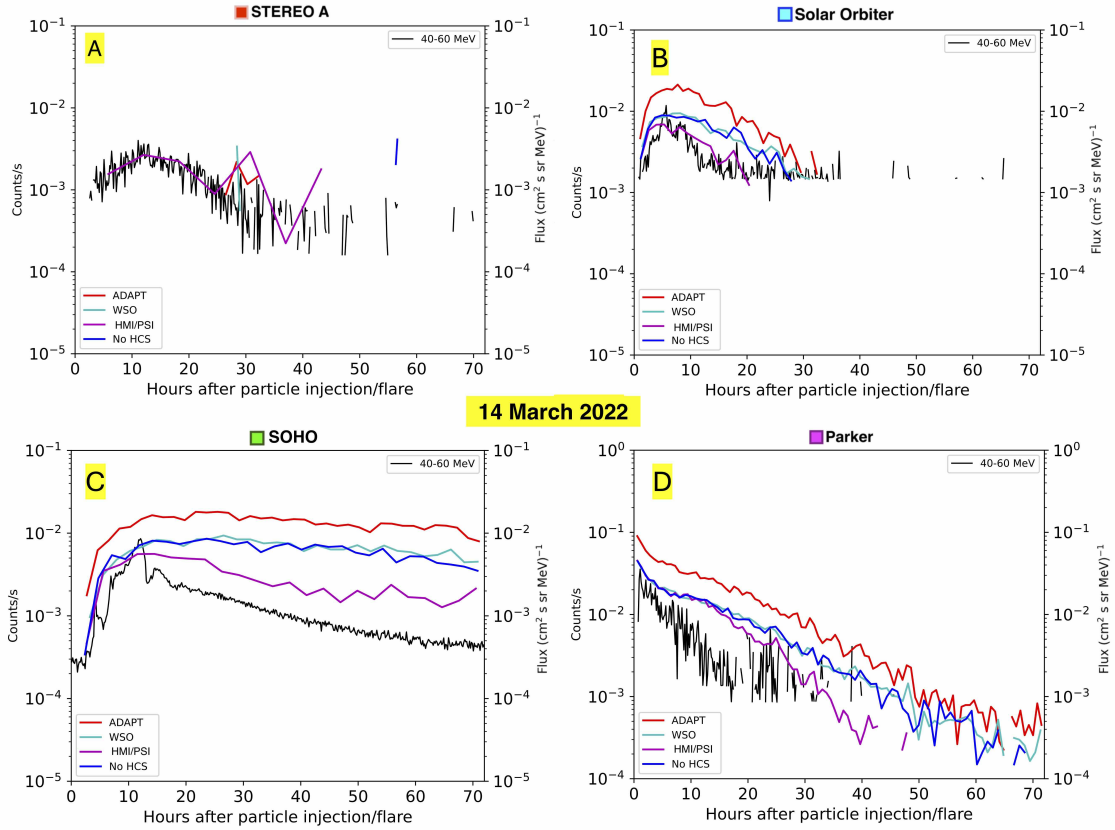

Figure 9. Observed flux profiles for 2022 March 14 (40–60 MeV) for (A) STEREO-A, (B) Solar Orbiter, (C) SOHO, and (D) Parker Solar Probe (black lines). Model flux profiles overlaid on each observer corresponding to HCS configuration: purple, HMI/PSI; red, ADAPT; cyan, WSO; blue, no HCS. All profiles are plotted for 72 hr from particle injection/flare start time. Model count rates and observed proton fluxes are labeled on the left- and right-hand vertical axes, respectively.

4.3.1. Observations and Modeled Flux Profiles

The modeled flux profiles at each observer location are shown in Figure 9, using the same energy channels as in Figure 5. Parker Solar Probe, located closest to the source region, recorded the earliest onset and highest peak flux in both observations and model results.

Observed intensities at STEREO-A are low and show a delayed and more gradual rise compared to Parker. Only the HMI/PSI HCS simulation results in particles at STEREO-A. This may reflect the relative inefficiency of particle transport along the HCS to STEREO's position, especially given that the source region lies offset from the HCS itself (see Figure 2).

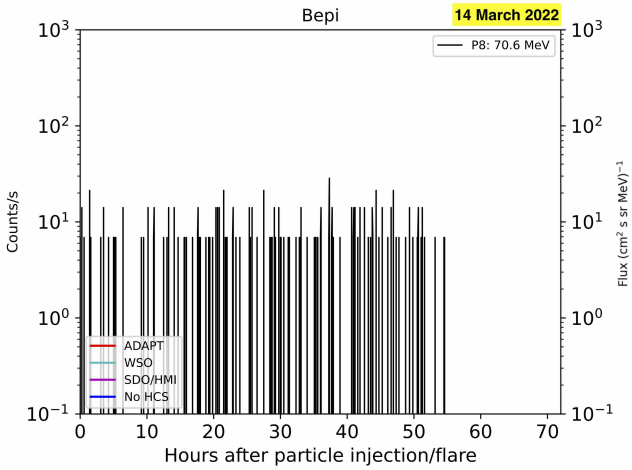

Figure 10. Observed (black) and model flux profiles (zero counts) for BepiColombo for 2022 March 14. Plot information is the same as in Figure 9.

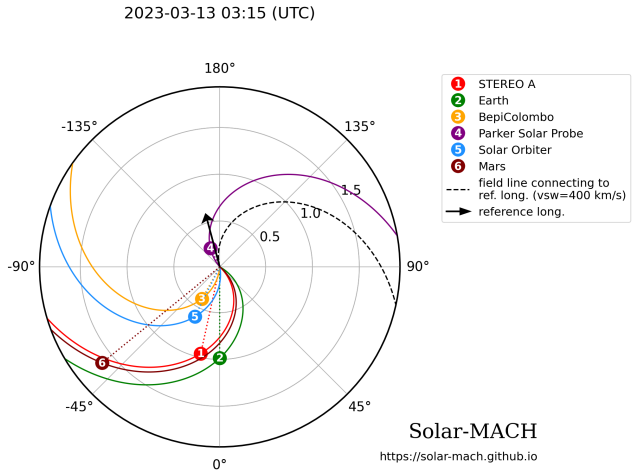

Figure 11. The longitudinal configuration of spacecraft (colored squares) and associated flare (black arrow) for the widespread SEP event of 2023 March 13, generated using the Solar-MACH online tool (J. Gieseler et al. 2023).

Among the three HCS models, the HMI/PSI configuration provides the best match to the observed flux profiles across these observers.

Figure 10 shows the modeled and observed profiles for BepiColombo. No significant event is seen in either data set. Although Bepi and STEREO share a similar longitudinal separation from the source region (Figure 7), only STEREO shows a modest increase in protons. This discrepancy may be explained by a combination of factors. First, Bepi's radial distance (0.46 au) differs from STEREO's (1 au), and second, the magnetic foot points of Bepi lie farther from both the source region and the HCS. As seen in Figure 2, Bepi's foot point lies on the opposite side of the HCS compared to the eruption site, while STEREO's is closer and better aligned. These differences likely hindered effective transport of particles to Bepi's location despite the similar longitudinal alignment.

4.4. 2023 March 13

The wide-longitude SEP event of 2023 March 13 originated from a solar eruption that began around 03:00 UTC, behind the eastern limb. The flare location is estimated as N24E168, based on an active region that had rotated out of view several days earlier (Carrington longitude estimated as 15–39 from AR13258; N. Dresing et al. 2025). A fast halo CME was observed with a peak speed of approximately 1699 km s^{-1}. Due to the rear-side location of the eruption and the viewing geometry of Solar Orbiter and Earth, no reliable flare magnitude was recorded. The spacecraft configuration at the time is shown in Figure 11.

Protons were first detected at Parker Solar Probe, followed by increases at STEREO-A and Earth. No significant event was observed at BepiColombo, which was both longitudinally distant and located at a heliocentric distance of 0.4 au. While Solar Orbiter and STEREO-A had similar longitudinal separations, their heliocentric distances were 0.71 au and 0.97 au, respectively. Parker, which was nearly aligned with the eruption site and located just 0.23 au from the Sun, observed the strongest event.

Figure 12 shows the cumulative 1 au proton crossing maps for all HCS configurations, as well as the no-HCS case. As expected, Parker shows the highest fluxes due to its close proximity to the injection site. The other five observers are more separated in longitude, with Earth the most distant. The number of particle crossings recorded at each observer varies significantly depending on the HCS configuration, underscoring the complexity of the field structure during this near–solar maximum period.

4.4.1. Observed and Modeled Flux Profiles

Figure 13 shows the observed and modeled flux profiles for each observer (again using the same energy channels as in the previous events). Parker Solar Probe exhibits the earliest onset and highest peak flux, in agreement with its favorable magnetic connection and close radial distance.

SOHO and STEREO-A show clear proton events in both observations and models, with similar rise times. These spacecraft, while longitudinally separated from the source, are located near the HCS in several configurations (see Figures 2 and 12), allowing for effective current sheet drift-driven transport.

In contrast, Solar Orbiter and BepiColombo show negligible increases in proton flux. While they are closer in both longitude and radial distance to the source than SOHO or STEREO-A, their foot points lie far from the HCS in all configurations (see Figure 2) and therefore are not magnetically well-connected to the injection site via the HCS. This highlights that proximity to the HCS, not simply longitudinal and radial distance from the source, is a key factor in determining whether an observer sees a SEP event.

Bepi's results are shown separately in Figure 14. As with 2022 March 14, no modeled counts are recorded here under any configuration. Given its large longitudinal separation, close-in radial distance, and foot point location far from the HCS, this result is consistent with the lack of an observed event.

Among the configurations tested, HMI/PSI again produces the best overall agreement with observations for Parker, STEREO-A, and SOHO.

During the event period, a second active region (AR13256) was present in the southern hemisphere (N. Dresing et al. 2025). While AR13258 (modeled above) is a more

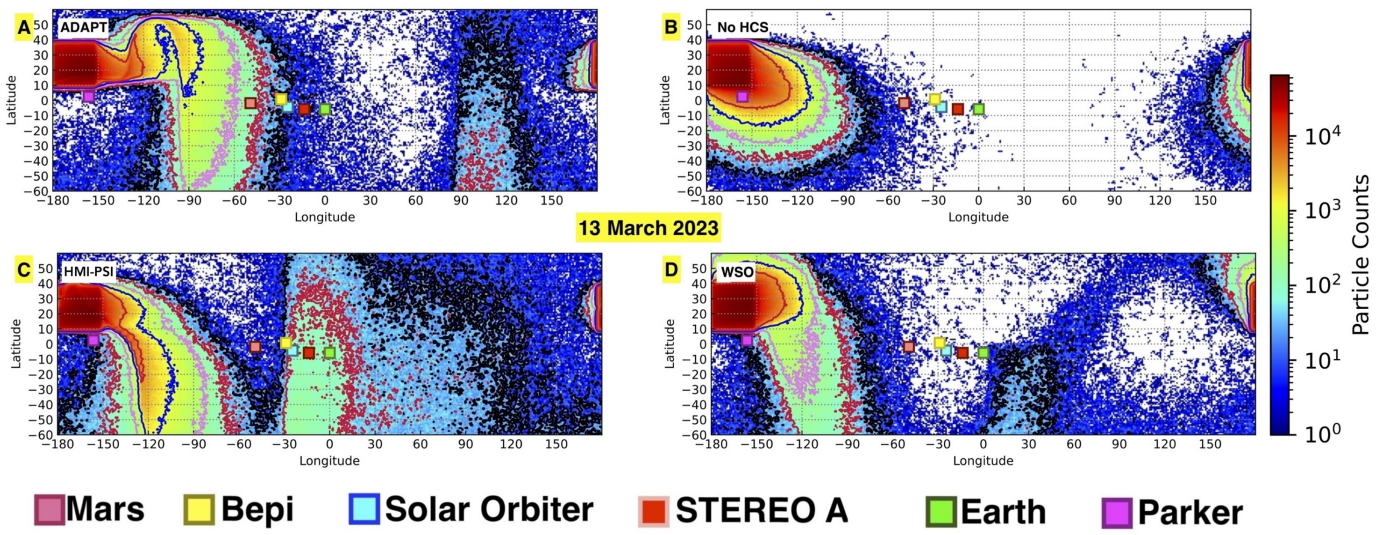

Figure 12. Cumulative 1 au proton crossing maps over 72 hr for (a) ADAPT HCS configuration, (b) no HCS, (c) HMI-PSI HCS, and (D) WSO HCS for 2023 March 13. Heliospheric observer locations are shown as colored squares: Bepi (yellow), Solar Orbiter (blue), STEREO-A (red), Earth (green), Parker Solar Probe (pink), Mars (brown). The injection location in each case is taken as the approximate location of the solar flare.

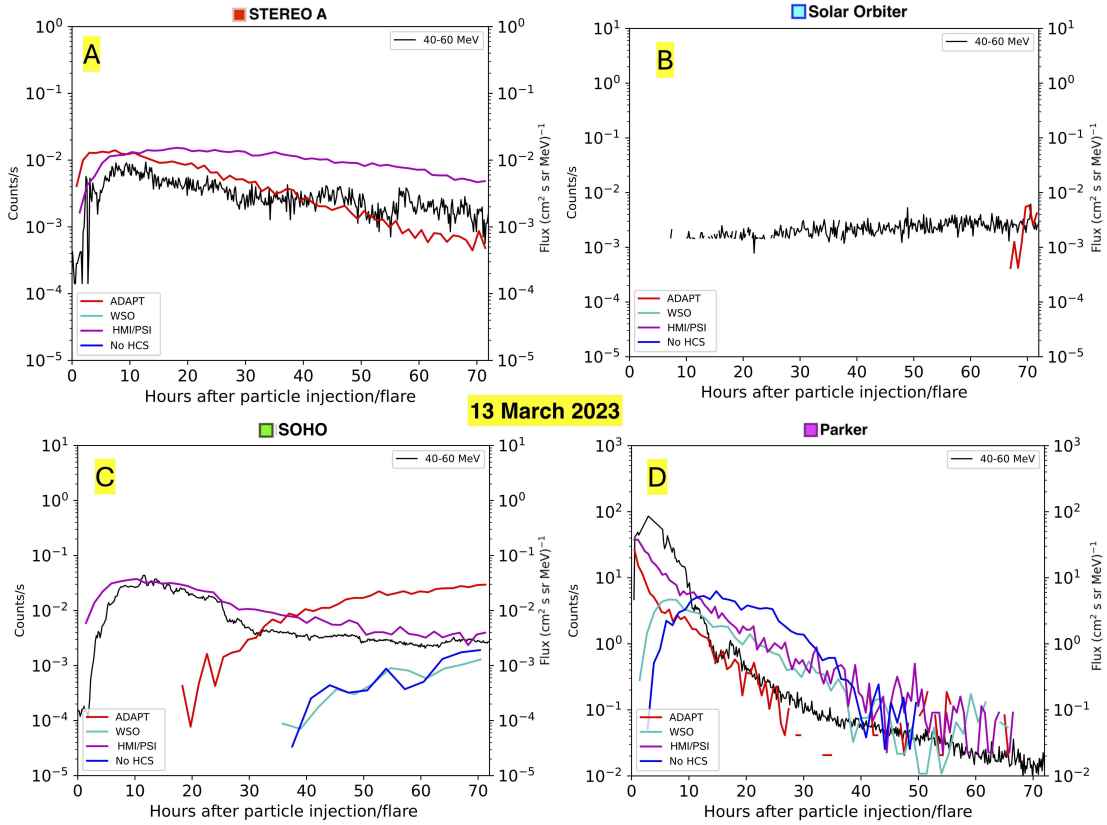

Figure 13. Observed 40–60 MeV proton flux profiles for 2023 March 13 for (A) STEREO-A, (B) Solar Orbiter, (C) SOHO, and (D) Parker Solar Probe (black lines). Model flux profiles obtained from the observers' heliopsheric location are overlaid on each plot corresponding to the HCS configuration: purple, HMI/PSI; red, ADAPT; cyan, WSO; blue, no HCS. Each plot shows flux profiles over 72 hr from time of injection/flare start time. Model count rates and proton flux rates are shown on the left and right vertical axes, respectively.

likely candidate due to its favorable magnetic connectivity and previously exhibited activity, we have performed additional simulations using this southern injection location. Across all HCS configurations, the modeled flux profiles showed no or minimal counts at all observers except the close-in Parker. This supports the conclusion supporting that AR13258 was the dominant particle source of the 2023 March 13 SEP event.

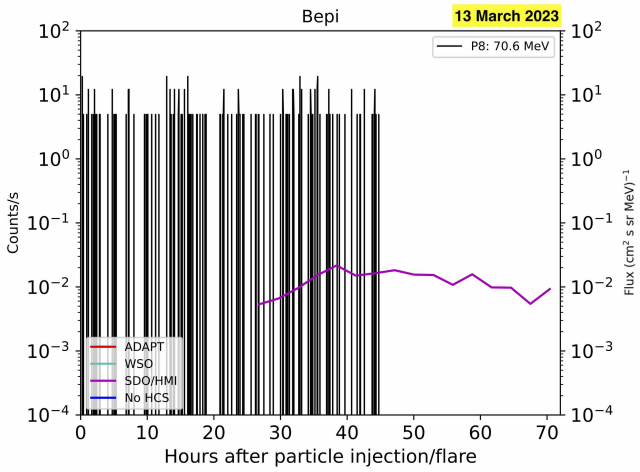

Figure 14. Observed (black) and model flux profiles for BepiColombo for 2023 March 13. Plot information is the same as in Figure 13.

5. Discussion and Conclusions

Modeling the HCS is inherently complex, particularly around solar maximum, when the HCS becomes increasingly warped and dynamic. In this work, we simulated three widespread SEP events from solar cycle 25 using a 3D test particle model and four different magnetic configurations: three HCS models (WSO, ADAPT, and HMI/PSI) and a case with no HCS included.

Across all events, the no-HCS model consistently underperformed, failing to reproduce observed particle fluxes at longitudinally distant observers. In contrast, the inclusion of an HCS enabled efficient particle transport across wide longitudes, often exceeding 180°, mainly via HCS drifts along the HCS structure. This result underscores the crucial role of the HCS in the propagation of energetic particles and highlights that even in events with fast, wide CMEs, interplanetary magnetic structure can strongly govern particle access across the heliosphere.

Each HCS configuration contributed differently to the modeled flux profiles. No single model was universally superior, but HMI/PSI provided the best overall agreement with observations across all three events, particularly for onset time, profile shape, and flux magnitude. WSO, although less detailed, performed reasonably well, demonstrating that the most effective HCS model may vary by event, observer, and phase of the solar cycle.

One of the most compelling cases was the 2023 March 13 event, where BepiColombo and Solar Orbiter were both closer in longitude and radial distance to the estimated injection region than Earth (see Figure 11) yet observed no significant SEP event. Earth, in contrast, registered clear flux enhancements. The key difference appears to be HCS proximity: Earth was magnetically closer to the HCS, while Bepi and Solar Orbiter had foot points far removed from it in all configurations. This finding reinforces the idea that observer distance from the injection site is not the only factor determining SEP access; proximity to the HCS can dominate, enabling long-range drift-driven transport even to otherwise poorly connected locations. Invoking a very broad injection region in this event (e.g., a wide CME-driven shock intercepting field lines to STEREO and Earth) would produce a SEP event at Bepi and Solar Orbiter; however, the latter two spacecraft did not observe SEPs.

In all three events, Parker Solar Probe consistently observed the highest peak fluxes and earliest onsets, attributable to its close proximity to both the Sun and the injection region. However, other observers (separated by over 180° in some cases) still detected significant SEP fluxes when their magnetic foot points lay near the HCS. This highlights the efficiency of HCS drift in redistributing particles across wide longitudes and suggests that the HCS plays a major role in shaping the global SEP event profile.

That said, the HCS is unlikely to be the sole mechanism at work. Extended injection durations, large shock geometries, and turbulent cross-field diffusion can all contribute to the broad spatial extent of SEP events. However, the instantaneous and spatially relatively compact injection used in our model isolates the effects of interplanetary transport. The fact that observed fluxes at distant observers are reproduced only when the HCS is included strongly supports its critical role, even in large events where other mechanisms may also be active.

Our model does not currently include perpendicular diffusion effects such as magnetic field line meandering, which are known to influence SEP propagation, particularly at lower energies and over longer timescales (e.g., T. Laitinen et al. 2016, 2023). These effects are not trivial to incorporate alongside an evolving HCS structure, and the interplay between turbulence and particle transport near the HCS remains poorly understood. Some studies suggest that HCS-driven transport dominates at higher energies and shorter timescales (e.g., T. Laitinen et al. 2016; S. Dalla et al. 2020; C. O. Waterfall et al. 2022), while turbulent diffusion becomes more relevant at later times or lower energies. Including both mechanisms simultaneously would be a valuable direction for future work, but doing so requires significantly more complex modeling. We have seen that models without an HCS and without perpendicular diffusion cannot reproduce the SEP distributions observed in the three events studied. However, we do not exclude the possibility that a model including only turbulence-based cross-field diffusion may achieve similar results, but this was not investigated here in order to isolate the role of the HCS.

Previous studies have reported that the HCS may act as a barrier to SEP transport, rather than a conduit. For example, K. Liou & C.-C. Wu (2024) conducted a superposed-epoch analysis of 319 Wind HCS crossings that revealed low-energy $<$10 MeV SEP channels often exhibited sharp flux decreases at the sheet, suggesting inhibited particle transport across the HCS.

These observations appear to contrast with our finding that the HCS enables efficient cross-field transport. However, we argue that such differences arise from the specific energy ranges, timescales, and transport regimes considered. Our simulations focus on $>$10 MeV protons, injected impulsively with negligible background turbulence. In this regime, drift motion dominates over diffusive cross-field transport, and the HCS serves as an effective channel for redistributing particles across longitudes, consistent with prior drift-based studies (E. H. Levy 1976; R. Burger et al. 1985; S. Dalla et al. 2020).

In contrast, the "barrier" behavior reported may reflect cases involving (1) lower-energy particles ($\leqslant$10 MeV), which experience slower, more stochastic transport (indeed, K. Liou & C.-C. Wu (2024) did not find similar SEP decreases

at higher energies), (2) differing IMF polarity, which alters drift direction and access pathways, or (3) field geometries in which the HCS lies between the source and observer but background turbulence is insufficient to scatter particles onto the sheet.

In our model, the HCS is treated as a smooth surface with a sharp magnetic polarity reversal. However, observational and theoretical work has shown that the HCS often contains complex internal structure (O. V. Khabarova & G. P. Zank 2017). This structure may play an important role in low-energy SEP transport by increasing scattering or distorting drift paths and should be considered in future, advanced models.

Ultimately, whether the HCS acts as a barrier or a conduit likely depends on a combination of particle energy, magnetic connectivity, IMF polarity, and the local structure of the sheet. Our results do not contradict barrier-like behavior in some regimes but instead demonstrate that for higher-energy SEP events, HCS drift plays a dominant and enabling role in achieving the observed longitudinal spread. A more complete understanding will require integrating both HCS geometry and microstructure with turbulence and time-dependent field evolution.

In summary, this study demonstrates that

1. The HCS is essential for reproducing observed SEP profiles at longitudinally distant observers, even in large, fast-CME events.
2. Different HCS models yield varying degrees of agreement with observations, with HMI/PSI providing the best overall performance.
3. SEP access is strongly dependent on an observer's magnetic proximity to the HCS, not just to the eruption site.
4. No-HCS models without field line diffusion cannot explain wide SEP distributions.
5. Turbulent processes and perpendicular diffusion, while not modeled here, are not expected to negate the dominant role of the HCS at higher energies and short timescales.

As solar maximum approaches and the HCS becomes increasingly dynamic, it is imperative that future models incorporate more accurate and high-resolution HCS configurations. Moreover, combining HCS-driven transport with other mechanisms such as field line meandering or extended shock acceleration will be key to building a more complete, predictive understanding of SEP event morphology.

Acknowledgments

This research is supported by the NASA Living With a Star Jack Eddy Postdoctoral Fellowship Program, administered by UCAR's Cooperative Programs for the Advancement of Earth System Science (CPAESS) under award 80NSSC22M0097.

S.D. acknowledges support from the UK STFC (grant ST/Y002725/1).

ORCID iDs

C. O. G. Waterfall https://orcid.org/0000-0003-4390-2920
G. A. de Nolfo https://orcid.org/0000-0002-3677-074X
D. da Silva https://orcid.org/0000-0001-7537-3539
S. Wallace https://orcid.org/0000-0002-1091-4688
S. Dalla https://orcid.org/0000-0002-7837-5780
J. G. Mitchell https://orcid.org/0000-0003-4501-5452

References

Altschuler, M. D., & Newkirk, G. 1969, SoPh, 9, 131
Arge, C., Luhmann, J., Odstrcil, D., Schrijver, C., & Li, Y. 2004, JASTP, 66, 1295
Arge, C., & Pizzo, V. 2000, JGRA, 105, 10465
Arge, C. N., Henney, C. J., Hernandez, I. G., et al. 2013, in AIP Conf. Proc. SOLAR WIND 13, 1539 (Melville, NY: AIP), 11
Arge, C. N., Odstrcil, D., Pizzo, V. J., & Mayer, L. R. 2003, in AIP Conf. Proc. SOLAR WIND TEN, 679 (Melville, NY: AIP), 190
Battarbee, M., Dalla, S., & Marsh, M. S. 2018a, ApJ, 854, 23
Battarbee, M., Guo, J., Dalla, S., et al. 2018b, A&A, 612, A116
Bieber, J. W., Droege, W., Evenson, P. A., et al. 2002, ApJ, 567, 622
Bieber, J. W., Evenson, P., Dröge, W., et al. 2004, ApJL, 601, L103
Bučík, R., Mason, G., Gómez-Herrero, R., et al. 2023, A&A, 669, A13
Burger, R., Moraal, H., & Webb, G. 1985, Ap&SS, 116, 107
Da Silva, D., Wallace, S., Arge, C., & Jones, S. 2023, SpWea, 21, e2023SW003554
Dalla, S., & Browning, P. 2005, A&A, 436, 1103
Dalla, S., de Nolfo, G. A., Bruno, A., et al. 2020, A&A, 639, A105
Dalla, S., Marsh, M., Kelly, J., & Laitinen, T. 2013, JGRA, 118, 5979
Dresing, N., Rodríguez-García, L., Jebaraj, I., et al. 2023, A&A, 674, A105
Dresing, N., Yli-Laurila, A., Valkila, S., et al. 2024, A&A, 687, A72
Dresing, N., Jebaraj, I., Wijsen, N., et al. 2025, A&A, 695, A127
Gieseler, J., Dresing, N., Palmroos, C., et al. 2023, FrASS, 9, 1058810
Gómez-Herrero, R., Dresing, N., Klassen, A., et al. 2015, ApJ, 799, 55
Harvey, J., Hill, F., Hubbard, R., et al. 1996, Sci, 272, 1284
Hoeksema, J. T., Wilcox, J. M., & Scherrer, P. H. 1983, JGRA, 88, 9910
Khabarova, O. V., & Zank, G. P. 2017, ApJ, 843, 4
Khoo, L., Sánchez-Cano, B., Lee, C., et al. 2024, ApJ, 963, 107
Kollhoff, A., Kouloumvakos, A., Lario, D., et al. 2021, A&A, 656, A20
Kota, J., & Jokipii, J. R. 1983, ApJ, 265, 573
Kouloumvakos, A., Papaioannou, A., Waterfall, C., et al. 2024, A&A, 682, A106
Kouloumvakos, A., Vourlidas, A., Rouillard, A. P., et al. 2020, ApJ, 899, 107
Laitinen, T., & Dalla, S. 2025, ApJ, 979, 106
Laitinen, T., Dalla, S., Waterfall, C., & Hutchinson, A. 2023, A&A, 673, L8
Laitinen, T., Kopp, A., Effenberger, F., Dalla, S., & Marsh, M. 2016, A&A, 591, A18
Levy, E. H. 1976, Natur, 261, 394
Liou, K., & Wu, C.-C. 2024, ApJ, 966, 16
Marsh, M. S., Dalla, S., Kelly, J., & Laitinen, T. 2013, ApJ, 774, 4
McGregor, S., Hughes, W., Arge, C., & Owens, M. 2008, JGRA, 113, A8
Mitchell, J., Cohen, C., Eddy, T., et al. 2023, ApJS, 264, 31
Mitchell, J., De Nolfo, G., Hill, M., et al. 2021, ApJ, 919, 119
Sáiz, A., Ruffolo, D., Rujiwarodom, M., et al. 2005, ICRC (Pune), 29, 229
Sánchez-Cano, B., Witasse, O., Knutsen, E. W., et al. 2023, SpWea, 21, e2023SW003540
Schatten, K. H. 1971, in Solar Wind, ed. C. P. Sonett, P. J. Coleman, & J. M. Wilcox (Washington, DC: NASA), 232
Schatten, K. H., Wilcox, J. M., & Ness, N. F. 1969, SoPh, 6, 442
Semkova, J., Koleva, R., Benghin, V., et al. 2023, LSSR, 39, 106
van den Berg, J., Strauss, D. T., & Effenberger, F. 2020, SSRv, 216, 146
Wang, Y.-M., & Sheeley, N., Jr. 1992, ApJ, 392, 310
Waterfall, C. O., Dalla, S., Laitinen, T., Hutchinson, A., & Marsh, M. 2022, ApJ, 934, 82
Worden, J., & Harvey, J. 2000, SoPh, 195, 247